Catalán-Martínez, D.; Santafé Moros, MA.; Gozálvez-Zafrilla, JM.; García-Fayos, J.; Serra Alfaro, JM. (2020). Characterization of oxygen transport phenomena on BSCF membranes assisted by fluid dynamic simulations including surface exchange. Chemical Engineering Journal. 387:1-15. https://doi.org/10.1016/j.cej.2020.124069

Characterization of oxygen transport phenomena on BSCF membranes assisted by fluid dynamic simulations including surface exchange

D. Catalán-Martínez[1], A. Santafé-Moros[2], J.M. Gozálvez-Zafrilla [2], J. García-Fayos[1], J.M. Serra[1,*]

[1] *Instituto de Tecnología Química, Universitat Politècnica de València – Consejo Superior de Investigaciones Científicas, Av. Naranjos s/n, 46022, Valencia, Spain*

[2] *Institute of Industrial, Radiophysical and Environmental Safety (ISIRYM), Universitat Politècnica de València, C/ Camino de Vera s/n, 46022, Valencia, Spain*

* jmserra@itq.upv.es

Abstract

The influence of fluid dynamic conditions on the oxygen transport through mixed ionic-electronic membranes was studied experimentally and numerically. A set of permeation experiments was performed in a wide range of operating conditions combining temperature, driving force and flow rate of air feed and sweep streams. A computational model was built and enabled to systematically evaluate the effect of the fluid dynamic conditions on O_2 separation process. This model includes the surface resistance (gas exchange kinetics) and bulk oxygen-ion diffusion. The experimental set was used to obtain the model parameters by following a two-step fitting procedure: a first fitting of a simplified one-dimensional model using genetic algorithms and a subsequent refining of the parameters using the complete model implemented in COMSOL Multiphysics. The high-accuracy model allowed characterizing the O_2 transport phenomena and understanding the different factors governing the overall process, e.g. by using different membrane thicknesses, sweep gases or vacuum. Simulations of the fitted model revealed the importance of the sweep effect in the O_2 transport across the membrane and enabled to establish rules for both design of permeation experiments and up-scaling.

Keywords: O_2 MIEC membrane, BSCF, CFD, permeation, modelling

1 Introduction

Oxygen Transport Membranes (OTM) represent a very appealing option for conducting an in-situ and low cost O_2 generation in small and medium-scale industrial applications with an O_2 demand, e.g. partial oxidation and combustions in cement, ceramic, glass and power generation industries [1–3]. Currently, these industries utilize vacuum pressure swing adsorption (VPSA) or cryogenic O_2 thus requiring a periodic bulk transport and storage implying a high cost and an external dependence. The economic and process advantages of implementing OTM-based O_2 supply systems have been largely studied, demonstrating benefits in O_2 production costs and a gain in process efficiency due to the thermal integration of OTM systems within processes presenting waste heat streams [4–6]. Amongst all the considered materials for OTMs, $Ba_{0.5}Sr_{0.5}Co_{0.8}Fe_{0.2}O_{3-\delta}$ (BSCF) is that presenting the highest permeation values with O_2 production capabilities of up to 62 $mL \cdot min^{-1} \cdot cm^{-2}$ at 1000 °C [7] despite the limited stability. Some studies have set a permeation threshold of at least 10 $mL \cdot min^{-1} \cdot cm^{-2}$ O_2 for considering the feasible utilization of OTM modules in oxy-fuel applications [8], therefore, membrane modules based on BSCF would be suitable for being integrated in such applications.

The configuration of OTM modules for integration within an industrial process can follow a 3-end or a 4-end approach [9]. In the latter, a hot gas stream belonging to the process (typically a flue gas stream) is used for heating up the module and for conducting the O_2 separation as sweep gas, whereas for the 3-end mode the permeated O_2 is collected by inducing vacuum. As BSCF is very sensitive to environments containing CO_2 and H_2O [10–12], it is considered a 3-end approach for BSCF-based OTM production systems. O_2 permeation performance is affected by several parameters such as temperature, O_2 concentration at feed and permeate sides, feed and sweep gas flow rates and membrane thickness. OTM module integration into an industrial process requires a preliminary design phase where plant layout, elements and devices are dimensioned. In this stage, process simulations are conducted for checking mass and energy transfer balances and thus perform the most precise definition of the different elements. Amongst all the existing equipment, the OTM module is the most difficult to simulate, since the most commonly used process simulation software do not include pre-defined algorithms for simulating the OTM module performance. It is then necessary to build an accurate permeation model that takes into account the aforementioned parameters as well as permeation mechanisms such as oxygen surface reactions and oxygen ions diffusion through the bulk material.

Regarding the development of these materials, modelling helps to improve the understanding of the permeation process as it provides a physical explanation from the raw empirical results. Therefore, the achievement of an accurate model describing the O_2 transport across the membrane is critical to design the assemblies for the demanded O_2 considering the suitable membrane area.

Most of the defined algorithms for these processes consider 0D models [13–16]. Modelling of O_2 permeation typically assumes local electroneutrality and the idealization of the ionic conduction and gas diffusion as hypothesis [17]. The applicability of the simulation results is limited by the considered assumptions. The most-frequently considered models are based on the surface reactions [18–24], chemical potential transport [13,25] and effective medium transport [26]. The development of these models allows the conduction of advanced studies by using computational techniques for higher analysis of the O_2 permeation process. On one side, commercial process simulation software such as Aspen Plus permits the evaluation of the process viability [9,27–34]. On the other side, Computational Fluid Dynamics (CFD) has been utilized as strong visualization tool to simulate the effects of reactions in membrane reactors and gas separation units [33,35,44–46,36–43]. In summary, although several of the developed models are suitable to numerous applications, the continuous development of O_2 permeation models is necessary especially when these membranes are integrated in reactive systems such as oxy-combustion reactors.

In the present work, the joint effect of the fluid dynamics conditions and operating conditions (feed concentration and temperature) on the oxygen transport was studied by using a model that specifically takes into account the most relevant phenomena involved in oxygen transport through MIEC membranes, i.e. formation and diffusion of oxygen vacancies and surface resistance to transport as proposed by Zhu et al. [13]. The model implementation was carried out using a Multiphysics software for finite element analysis (COMSOL Multiphysics) that made possible to handle complex geometries. The results herein obtained will permit the understanding and interpretation of the different factors governing the oxygen permeation and subsequently, the definition of strategies for the optimization of the oxygen production with ceramic MIEC materials. Therefore, the main objective of this work is providing a tool for researchers on the definition of tests and interpretation of experimental results involving permeation of oxygen, as well as helping of more advanced and applied research oriented to the design and the upscaling of processes in the field of OTM technology.

2 Materials and methods

2.1 Experimental procedure

In order to obtain the necessary information to fit the membrane parameters from experimental data, permeation experiments were carried out in an experimental set-up for a wide range of operating conditions (i.e. temperature, flow rates, O_2 partial pressure, sweep gas type). Permeation tests were conducted on 0.8 mm-thick disk-shaped BSCF membranes. Dense membrane specimens were produced from $Ba_{0.5}Sr_{0.5}Co_{0.8}Fe_{0.2}O_{3-\delta}$ commercial powder (IKTS Fraunhofer, Germany) after uniaxial pressing in a 26 mm diameter steel die and subsequent sintering at 1100 °C in air for 5 hours. These samples were tested in a quartz lab-scale reactor in which synthetic

air (21%, vol. O_2) or O_2/N_2 mixtures were fed into the O_2-rich chamber, while Ar was used as sweep gas on the permeate side chamber in a 4-end mode configuration, as displayed in Figure 1a-b. Both streams were fed at atmospheric pressure. Inlet gases were preheated in order to ensure the correct gas temperature for contact with the membrane surface. This is particularly important when high gas flow rates are employed. All streams were individually mass flow controlled. The temperature was measured by a thermocouple attached to the membrane. Membrane gas leak-free conditions were achieved using gold rings, which were heated to 1060 °C for 4 h immediately prior to the measurement. The permeate was analyzed at steady state by online gas chromatography using a micro-GC Varian CP-4900 equipped with Molsieve5A, Pora-Plot-Q glass capillary, and CP-Sil modules. Membrane gas leak-free conditions were ensured by continuously monitoring the N_2 concentration in the product gas stream. An acceptable sealing was achieved when the ratio between the O_2 flow leak and the O_2 flux was lower than 1%. The data reported here were achieved at steady state after 1 h in the reaction stream. Each test was repeated three times to minimize the analysis error. The experimental analytical error was below 0.5%.

A one-dimensional implementation of the model was additionally performed for diminishing the computational time required for fitting. This enabled an objective function performing significantly faster than the objective function for the multidimensional model considering the exact system geometry. Therefore, it was possible to use a genetic algorithm for the minimization of the objective function, a technique which is suitable for seeking for global optima, but highly time-consuming. Once the model parameters were fitted, the model was able to predict the O_2 permeation flux using as inputs the O_2 partial pressure on both sides of the membrane and the operating conditions. Subsequently, the fitting parameters obtained with the one-dimensional model were used as starting point for the minimization of the objective function based on the full set-up geometry (COMSOL model) by using a direct optimization method.

Once the fitting of the parameters was performed in the COMSOL model for a base case, the effects of membrane thickness, feed and sweep flow were studied in a range around reference conditions. The subsequent results will be displayed either as mapping profiles or as 2D dimensionally-averaged values on the membrane plane. In addition, the effect of dilution and shear conditions in the sweep side and the study of the limiting case of sweep vacuum conditions were thoroughly characterized. Finally, it was built a specific permeation model for the considered setup geometry by using dimensionless numbers and the whole set of CFD results.

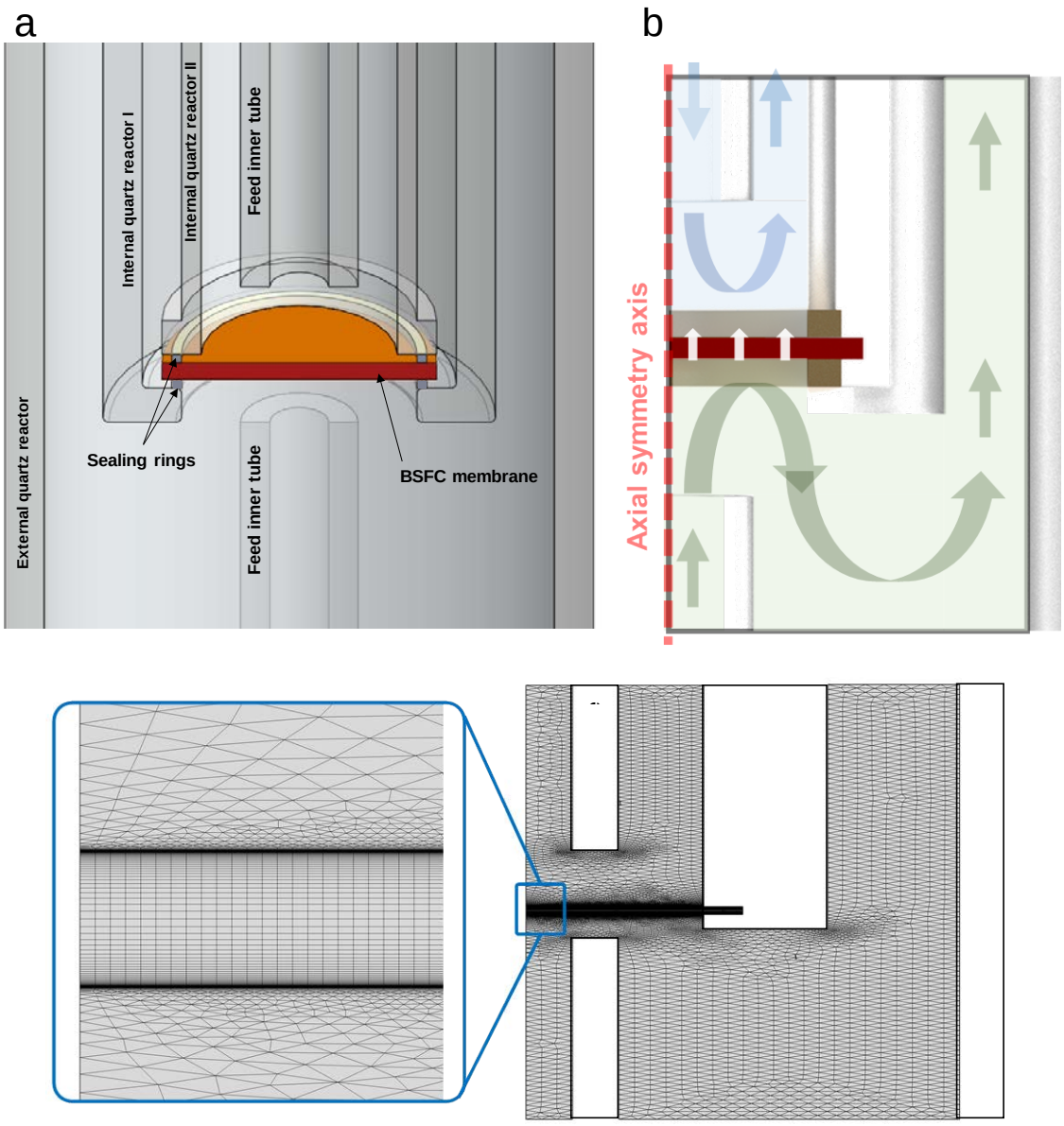

Figure 1. Experimental set-up. (a) View of the general set-up; (b) adaptation of the geometry to 2D axial symmetry; (c) mesh of the geometry for the CFD method

2.2 Modeling procedure

2.2.1 Model equations

The developed model describes the O_2 transport through a MIEC membrane taking into account bulk diffusion and surface resistances, both based on empirical parameters, together with model equations that account for fluid dynamics and component transport in gaseous phases, assuming isothermal conditions. Note that these equivalent resistances are defined as a degree of the limitation of the transport through the membrane surfaces but are not related to true electric resistance or charge polarization phenomena. Table 1 summarizes the equations used to describe the transport through the membrane bulk and across the gas-membrane interfaces. According to

the simplified scheme shown in Figure 2, five regions are distinguished, where the O_2 flux is expressed in a different manner as a function of the oxygen potentials in each region.

The O_2 transport through the membrane bulk occurs through the diffusion of oxygen vacancies (Eq. (1)). In this equation, the diffusion coefficient of oxygen vacancies is assumed to follow an Arrhenius behavior (Eq. (2)). The equilibrium between the effective O_2 pressure on the gas side and the oxygen vacancies (oxygen non-stoichiometry) is expressed by a Langmuir-like equation (Eq. (3)) with temperature-dependent coefficients (Eq. (4)) and (5)). This set of equations together with Eq. (6) enables to relate the concentration of oxygen vacancies on the membrane surfaces with the respective effective O_2 pressure of each side.

The transport of O_2 in the gaseous phases depends on the fluid dynamics. In the model, the Navier–Stokes equations were used under the assumptions of stationary and isothermal flow, negligible volume forces, density independent from composition, and Newtonian gas behavior. The O_2 transfer in the feed gas was modeled using the Maxwell–Stephan diffusion approach, as the O_2 fraction is far from dilute conditions. This equation requires the estimation of the diffusivity matrix in terms of binary diffusion coefficients. In the sweep-gas compartment, as the O_2 concentration is low, the Fick's law accurately describes the O_2 mass transfer in the gas phase. The binary diffusion coefficients were obtained from the Chapman-Enskog theory as a function of the temperature and molecular properties. The flow modelling and transport equations used in the COMSOL model are described in a previous work. [47]

The flux on both membrane interfaces is proportional to the drop in chemical potential and inversely proportional to the transport surface resistances (r_f) and (r_p) in Eqs. (11) and (12), respectively. The drop in chemical potential through the membrane-gas interface is calculated with the O_2 effective pressure (in equilibrium with the concentration of oxygen vacancies in the membrane) and the gas O_2 pressure in contact with the membrane (Eqs. (7) - (10)). According to the surface resistance model proposed by Zhu et al. [13] , the resistances follow a pressure power-law (Eqs. (13) and (15)) with coefficient $n = 0.5$. The specific resistances of the feed side ($r_{f,0}$) and permeation side ($r_{p,0}$) followed an Arrhenius-like expression (Eqs. (14) and (16)).

In the case of the one-dimensional implementation of the model, it was assumed that the only relevant gradients were those along the axial coordinate z. The equations resulting from this simplification are shown in Table 2. Thereby, the diffusive flux of oxygen vacancies from permeate to feed side is simplified by Eq. (17), where the surface-averaged value of oxygen vacancies concentrations for each side depends on the average oxygen effective pressure in each membrane side. In this case, the Navier-Stokes and the rigorous transport equations cannot be used to obtain the O_2 transport in the gas phase domains. Instead, these equations were replaced by phenomenological expressions using a mass transfer coefficient (Eq. (23), (24)). Note that the

latter equation considers an average O_2 pressure in the permeate compartment being expressed in its implicit form. In both equations, the mass transfer coefficients k_f and k_p were obtained from mass transfer simulations performed with the Multiphysics software for the gas compartments specific geometries as a function of gas inlet flow, temperature and gas composition.

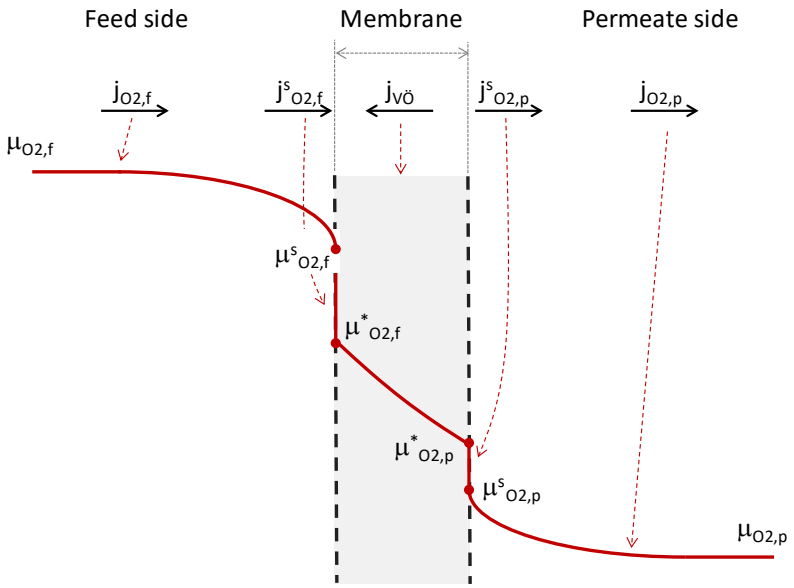

Figure 2. Scheme of the oxygen chemical potential gradient for the oxygen permeation process through the MIEC membrane

Table 1. Model equations

$$j_{V_{\ddot{O}}} = -D_{V_{\ddot{O}}} \nabla C_{V_{\ddot{O}}}$$	(1)
$$D_{V_{\ddot{O}}} = A_v \exp\left(-\frac{E_{a,v}}{T}\right)$$	(2)
$$\delta = \frac{3\,K\,(P_{O2}^{*} \cdot P_0^{-1})^m}{1 + K\,(P_{O2}^{*} \cdot P_0^{-1})^m}$$	(3)
$$\ln K = C_1 - \frac{C_2}{T}$$	(4)
$$m = C_3 + C_4\,T$$	(5)

$$C_{V_{\ddot{o}}} = \frac{\delta}{v_{BSCF}}$$	(6)
$$\mu^{s}_{O_2,f} = R\ T\ \ln\left(P^{s}_{O_2,f} \cdot P_0^{-1}\right)$$	(7)
$$\mu^{*}_{O_2,f} = R\ T\ \ln\left(P^{*}_{O2,f} \cdot P_0^{-1}\right)$$	(8)
$$\mu^{*}_{O_2,p} = R\ T\ \ln\left(P^{*}_{O2,p} \cdot P_0^{-1}\right)$$	(9)
$$\mu^{s}_{O_2,p} = R\ T\ \ln\left(P^{s}_{O_2,p} \cdot P_0^{-1}\right)$$	(10)
$$j^{s}_{O_2,f} = \frac{1}{4^2\ F^2} \cdot \frac{\mu^{s}_{O_2,f} - \mu^{*}_{O_2,f}}{r_f}$$	(11)
$$j^{s}_{O_2,p} = \frac{1}{4^2\ F^2}\ \frac{\mu^{*}_{O_2,p} - \mu^{s}_{O_2,p}}{r_p}$$	(12)
$$r_f = r_{f,0} \cdot \left(\frac{P_{O_2,f}}{P_0}\right)^{-\frac{1}{n}}$$	(13)
$$r_{f,0} = A_f \exp\left(-\frac{E_{a,f}}{T}\right)$$	(14)
$$r_p = r_{p,0} \cdot \left(\frac{P_{O_2,p}}{P_0}\right)^{-\frac{1}{n}}$$	(15)
$$r_{p,0} = A_p \exp\left(-\frac{E_{a,p}}{T}\right)$$	(16)

Table 2. Simplified equations used for the unidimensional model

$$j_{V_{\ddot{O}}} = -D_{V_{\ddot{O}}} \frac{C_{V_{\ddot{O}}}\Big|_{z=0} - C_{V_{\ddot{O}}}\Big|_{z=\Delta z}}{\Delta z} \quad (17)$$

$$j_{O_2,f} = k_f \cdot \frac{P_{O_2,f} - P^s_{O_2,f}}{R\,T} \quad (18)$$

$$j_{O_2,p} = k_p \cdot \left[\frac{P^s_{O_2,p}}{R\,T} - \left(\frac{P_{O_2,p}}{R\,T} + \frac{j_{O_2,p} \cdot A_{mod}}{2\,Q_p}\right)\right] \quad (19)$$

2.2.2 Boundary conditions

The solution of the system of equations requires imposing proper conditions at the boundaries of the five considered regions. For the outmost boundaries, the pO_2 in the feed and sweep gas bulk must be imposed. For the innermost boundaries, flux-matching conditions at the gas-membrane interfaces were used (Eqs. (20) and (21)). At the feed side membrane surface (z=0), the flux from the feed gas must be equal to O_2 flux in terms of the surface resistance to transport (defined by Eq. (11)) and the O_2 flux caused by the filling of oxygen vacancies at the membrane surface (Eq. (20)). On the other side of the membrane (z=Δz), the O_2 flux originated by the formation of oxygen vacancies must equate the flux given by Eq. (12) and the O_2 flux from the gas in contact to the membrane side to the sweep-gas bulk (Eq. (21)).

$$j_{O_2,f}\Big|_{z=0} = j^s_{O_2,f} = \frac{1}{2}\, j_{V_{\ddot{O}}}\Big|_{z=0} \quad (20)$$

$$\frac{1}{2}\, j_{V_{\ddot{O}}}\Big|_{z=\Delta z} = j^s_{O_2,p} = j_{O_2,p}\Big|_{z=\Delta z} \quad (21)$$

In the case of the simplified one-dimensional approach, as there are not any flux components different from the axial one, all the fluxes for Eq. (11), (12), (17), (18) and (19) are equal.

2.2.3 Model calculation

The equations of the multidimensional model (Table 1) were implemented in the software COMSOL Multiphysics v4.4. As the axial geometry permits using 2D computational domains, then the model complexity can be greatly reduced from a computational point of view if only radial and z-components of the equations are considered [47]. Therefore, three interconnected domains were considered: permeate, membrane, and feed compartments.

Figure 1c shows the meshing built for the different domains. The membrane domain used a mesh based on quadratic elements using a mapped mesh type, while the gas phases were meshed using free triangular elements. For the boundary layers, a special type of meshing suitable for contours was used. The final mesh has an average quality mesh of 0.9316. The calculations were carried out using the Parallel Direct Solver (PARDISO) with parameter continuation to warrantee convergence, fixing the tolerance of the method at 0.001.

The simplified one-dimensional model was implemented in MATLAB and used the software numeric capabilities to solve the set of non-linear algebraic equations corresponding to the flux identity between domains. All scalar equations of Table 1 were used in the one-dimensional model. The expression for flux of oxygen vacancies was simplified to Eq. (12). The flux equations were expressed as a function of the inlet O_2 pressure, O_2 pressure in the gas in contact with the membrane surface and effective pressure in equilibrium with the oxygen vacancies. The application of the boundary equations required the calculation of these pressures and, consequently, of the O_2 fluxes.

2.3 Fitting procedure

The model equations include many parameters. To simplify the problem, the equilibrium related parameters of Eqs. (4) and (5) were taken from [48]. Even so, the amount of the remaining temperature dependent parameters was high. However, the quantity of parameters to be fitted becomes smaller if the fitting is performed independently for each temperature. Once the parameters for each temperature are obtained, they can be fitted to determine their temperature-dependent correlations.

According to this procedure, the experiments were divided into subsets for each temperature. Figure 3 schematizes a procedure for the fitting of the parameters to the set of experimental results. However, this fitting procedure has the problem that many local minima can occur. To increase the possibilities to obtain a global optimum, optimization technique based on genetic algorithms was used although a large number of evaluations of the objective function were required. This optimization approach can be very time-consuming in the case of 2D models solved by a Multiphysics software.

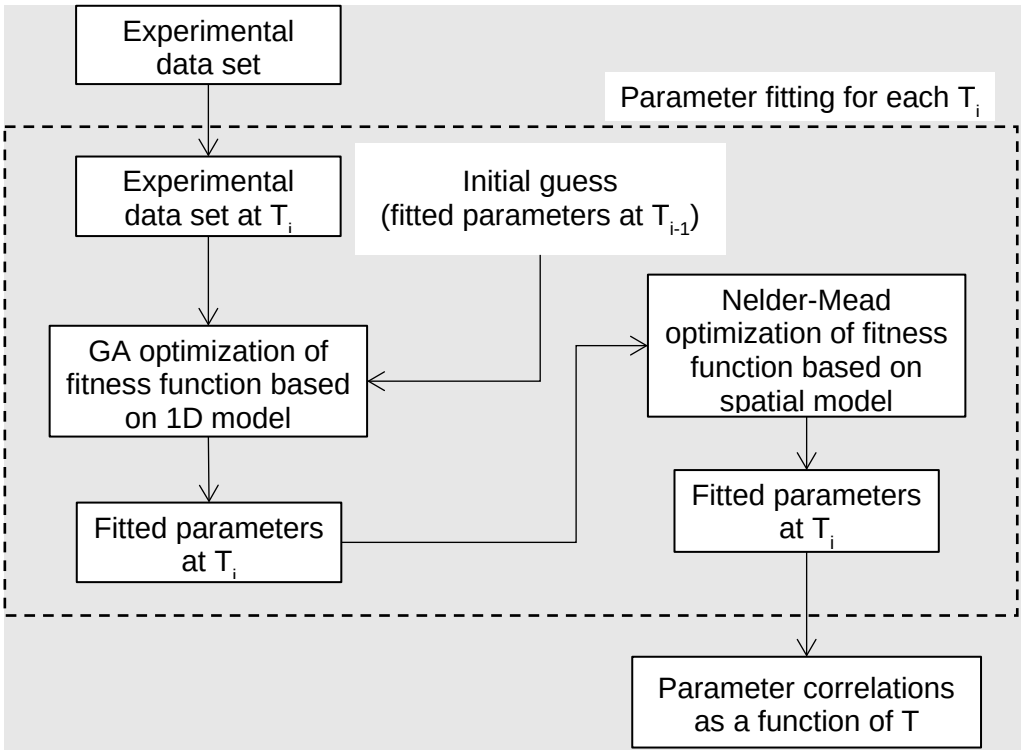

Figure 3. Overall fitting procedure of the model parameters

The genetic algorithm used was a single genetic algorithm for real-coded parameters as described by Haupt and Haupt [49]. The individuals took the form of the parameter vector to be fitted and the objective function to be minimized was the medium square error (MSRE, Eq (22)) obtained between the calculated values for the present parameter vector and the experimental values at constant temperature. The algorithm starts from an initial population randomly generated. The initial population size was 45. The population was improved for a number of generations of 800.

The values of the parameters obtained using the one-dimensional model were used as starting values for the fitting procedure using an objective function based on the 2D model. In this case, a direct method (Nelder-Mead) was sequentially applied to minimize the objective function by sequentially using the results given by COMSOL. The whole procedure was repeated for each temperature. Afterwards, linear fitting was applied between the logarithm of the parameters and the inverse of temperature to obtain the law of temperature dependence for each parameter. The fitting procedure of the vector of parameters was based also on the minimization of the medium square relative error (MSRE) of the oxygen flux at given operating conditions (Eq (22)).

$$MSRE(\vec{p}) = \frac{1}{N}\sum_{i}^{N}\left(1 - \frac{j_{O2,i}^{calc}(\vec{p},\vec{y}_i)}{j_{O2,i}^{exp}}\right)^2 \quad (22)$$

2.4 Simulation studies

By using the fitted parameters, several studies were performed in order to analyze the influence of the main variables of the membrane and separation process. In addition, the use of vacuum pressure was studied as an alternative to using a sweep gas for many industrial applications. The conditions of the reference case used in the simulations are shown in Table 3. In the following sections, the specific conditions and ranges studied are described while keeping the rest of the conditions as depicted in Table 3.

Table 3: Conditions for the reference case

Parameter	Units	Values
Feed inlet composition	-	Air
Feed inlet flow	mL_{STP}/min	300
Pressure in the feed compartment	bar	1
Sweep inlet composition	-	Ar[(1)]
Sweep inlet flow	mL_{STP}/min	300
Pressure in the sweep compartment	bar	1
Membrane thickness	μm	800
Temperature	°C	700, 800, 900, 1000

[(1)]Ar with $2 \cdot 10^{-5}$ bar of O_2

2.4.1 Effect of the membrane thickness

The membrane thickness was varied from 10 μm to 10000 μm to assess the relative importance of the bulk transport with respect to the other transport mechanisms involved in O_2 separation. The study was performed with and without considering surface-exchange resistances.

2.4.2 Effect of the feed inlet flow

The flow rate of the air feed was varied from 10 to 1250 mL_{STP}/min to characterize the fluid dynamic behavior in the feed compartment and to determine its impact in the O_2 flux as a function of temperature.

2.4.3 Effect of the sweep inlet flow

The gas sweeping causes different effects that influence the magnitude of the net O_2 flux. Namely, the gas sweeps the O_2 from the membrane surface and simultaneously dilutes the swept O_2 gas. Both effects enable to increase the driving force for oxygen transport. Both effects were investigated through the fluid-dynamics simulation in the permeate (sweep gas) compartment, i.e. by varying the sweep inlet flow rate in the range from 10 to 1000 mL_{STP}/min.

2.4.4 Effect of the sweep gas composition

He, CO_2 and steam were used as sweep gases for comparison with the reference gas (Ar). For all the three sweep gases, a pO_2 of $2 \cdot 10^{-5}$ bar was assumed at the inlet. CO_2 and steam may be adsorbed on the BSCF membrane surface, leading to changes in the O_2 surface-exchange kinetics and in the material microstructure, thus affecting negatively the O_2 permeation [9,11,12,50,51]. However, the model does not consider this specific surface phenomena and, therefore, the simulation only will account for fluid dynamic effects related with molecular mass, viscosity and differences of oxygen diffusion in these gases.

2.4.5 Activation energy

Taking into account the simulation results obtained by varying the feed and sweep inlet flow rates, two situations according to the magnitude of the concentration polarization were studied for all sweep gases: (i) situation with relative low sweep gas flow; and (ii) situation of high sweep gas flow, i.e. the effect of concentration polarization may be negligible. The term polarization here is used as the situation where substantial gas concentration gradients are present in the gas diffusion chambers. The comparison of both situations made possible to determinate the effect of the concentration polarization on oxygen flux and the associated (apparent) activation energy. Indeed, the apparent activation energy is usually determined experimentally and is used as a good indicator of the most probable rate-limiting step in O_2 separation with ionic membranes.

2.4.6 Fluid-dynamic dimensionless studies

The analysis of the CFD results on the effect of the sweep gas in the oxygen transport across the membrane was made considering correlations of dimensionless numbers. For this kind of processes where the permeation is governed by the oxygen transference through the membrane, a correlation is needed to describe gas transference, gas diffusions and fluid-dynamics. The typical correlation for this kind of phenomena uses (Eq (23)) [52–57], which relates the Sherwood number $\left(Sh = \frac{k_m \cdot L_c}{D}\right)$, Reynolds number $\left(Re = \frac{\rho \cdot u \cdot L_c}{\mu}\right)$ and Schmidt number $\left(Sc = \frac{\mu}{\rho \cdot D}\right)$.

$$Sh = \mathrm{a} \cdot Re^{\mathrm{b}} \cdot Sc^{\mathrm{c}} \tag{23}$$

Where a, b, and c are the constants of the correlation. A typical value for c for this correlation is 1/3. The material transference coefficient (k_m) was measured considering:

$$J_{O2} = \mathrm{k}_m \cdot \Delta C_{O2} \tag{24}$$

$$k_m = \frac{J_{O2}}{\Delta C_{O2}} \tag{25}$$

Where ΔC_{O2} is the oxygen concentration gradient in the surroundings of the membrane. For the feed chamber: $\Delta C_{O2,feed} = C_{O2,chamber} - C_{O2,memb}$; and for the sweep chamber: $\Delta C_{O2,sweep} = C_{O2,memb} - C_{O2,chamber}$.

2.4.7 Vacuum extraction system

The simulation of a vacuum extraction system in the same set-up required the implementation of several changes in the model. The sweep gas inlet was removed, and the sweep gas outlet was replaced by the vacuum simulation module included in the COMSOL software at the corresponding pressure. The composition of the compartment was adapted according to O_2 properties. The considered vacuum pressures ranged from 10 to 200 mbar. The feed inlet for all cases was 500 mL_{STP}/min of standard air.

3 Results

3.1 Fitting of the CFD model

Figure 4 shows the fitting results for parameters of the CFD model as a function of temperature. The diffusion coefficient of oxygen vacancies (D_v) fits an Arrhenius expression (Figure 4a) with a correlation factor of > 0.99. A comparison with diffusion coefficients from previous reports is available in Figure S3. The temperature dependence of the parameters associated to gas-exchange surface resistance (Figure 4b) was different for each membrane side. In the case of the feed – membrane surface, the resistance parameter r_f decreases with temperature and the results fit to an Arrhenius equation (Figure 4b). For the membrane – sweep surface, the resistance parameter r_p decreases until 800 °C, and it almost stabilizes its value above this temperature. The results after fitting to an Arrhenius expression are shown in Table 4. The activation energy values of D_v are similar to those obtained elsewhere but the surface resistances present lower values because of a small pre-exponential factor [24,58–63]. The decrease of the resistance related to the oxygen surface exchange indicates an intensification of this phenomenon (in both sides of the membrane when the temperature increases). The improvement of the surface exchange with temperature was previously reported [24,59,61].

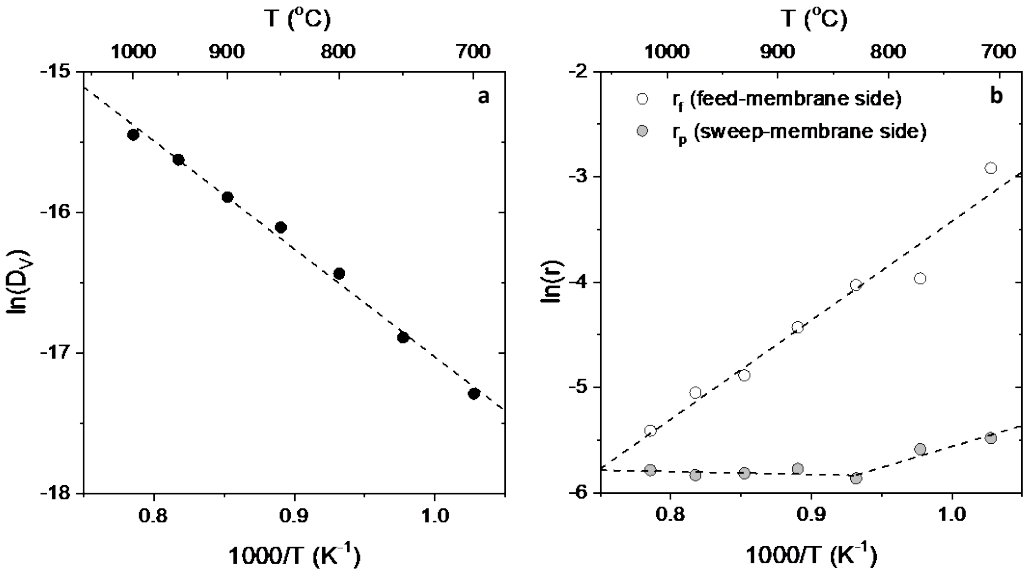

Figure 4: Fitting results (a) diffusion coefficient of oxygen vacancies (b) Pre-exponential factors for surface resistances of the CFD model.

Table 4. Parameter fitting of the CFD model as an Arrhenius function of the temperature: $f(T) = \mathrm{A} \cdot \exp\left(-{}^{Ea}/_{\mathrm{R}T}\right)$

Coefficient	**Pre-exponential factor**	**units**	**Activation energy, E_a**	**Units**
$\boldsymbol{D_{Vo}}$	8.471E-5	m^2/s	63.853	kJ/mol
$\boldsymbol{r_{f,0}}$	2.700E-6	$\Omega \cdot cm^2$	-78.133	kJ/mol
$\boldsymbol{r_{p,0}}$ **(T < 800 °C)**	7.223E-5	$\Omega \cdot cm^2$	-33.035	kJ/mol
$\boldsymbol{r_{p,0}}$ **(T > 800 °C)**	3.770E-3	$\Omega \cdot cm^2$	2.272	kJ/mol

Figure 5 compares the experimental results (data points) of O_2 flux (J_{O2}) with model simulations (solid lines) using the fitted parameters as a function of the pO_2 of each chamber. In the studied range, the experimental data have similar values to those reported in other works [62,64–69] for BSCF membranes. In Figure 5a, the pO_2 of the feed inlet is varied at different temperatures while the sweep inlet composition remains fixed, as can be seen, the obtained CFD model fits the experimental results with a high degree of accuracy. Similarly, Figure 5b illustrates the goodness of the fitting when the pO_2 of the sweep gas is varied at a fixed feed inlet composition.

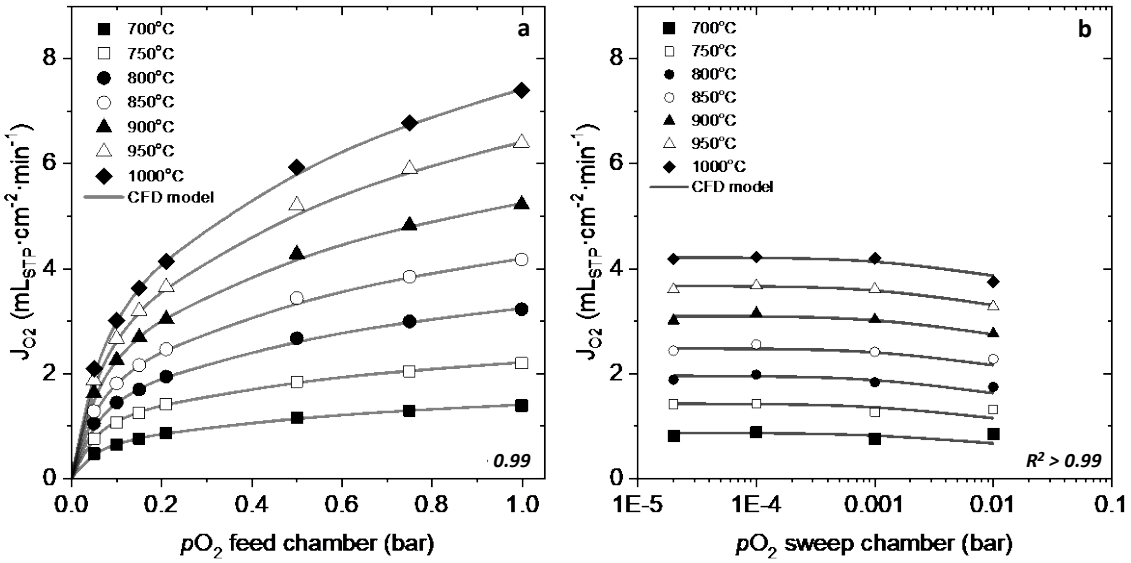

Figure 5: Comparison of experimental results (points) and model simulations using the fitted parameters (full lines) for oxygen flux at different temperatures (a) Effect of the oxygen partial pressure of the feed inlet; (b) Effect of the oxygen partial pressure of the sweep gas inlet (feed inlet conditions: air, 300 mL_{STP}/min; sweep inlet conditions: argon, 300mL_{STP}/min, membrane thickness: 1mm).

4 Results of the CFD simulations of the 3D permeation setup

4.1 Effect of membrane thickness:

As a rule of thumb, the higher the membrane thickness the higher the bulk-transport resistance towards O_2 permeation, hence an improvement in J_{O2} can be expected when reducing thickness as long as the bulk-transport governs the O_2 separation. Figure 6 shows the J_{O2} calculated by using the CFD model from the fitted parameters as a function of the membrane thickness at different temperatures. On one hand, if gas-exchange surface resistances are considered in addition to bulk-transport resistances, J_{O2} does not increase (solid lines) when reducing membrane thickness below 100 µm. On the other hand, if the effect of surface resistance is neglected in the model and only bulk-transport is considered, the flux increases as the membrane thickness is decreased in the considered range. Therefore, for thicknesses around 100 µm, the surface resistances fully control the permeation process, with no beneficial effects in J_{O2} if thickness is reduced. At thicknesses above 100 µm, both model considerations lead to a similar J_{O2} behavior with a performance worsening with thickness increments since the process is mainly controlled by the bulk transport of oxygen vacancies. Furthermore, for thicknesses higher than 2 mm, the bulk diffusion governs the oxygen permeation. These results are in agreement previous reports [70].

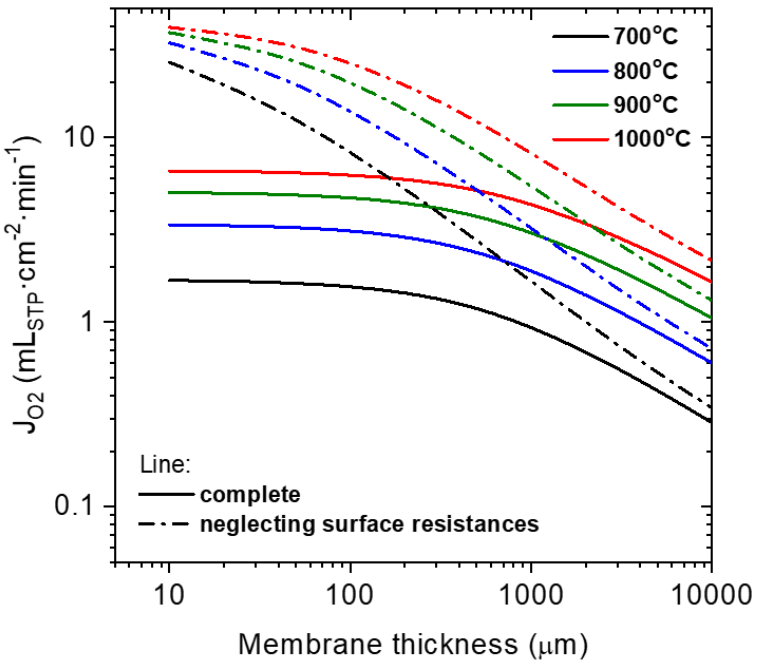

Figure 6: Effect of thickness on the average oxygen flux (Feed inlet conditions: air, 300mL_{STP}/min; sweep inlet conditions: argon ($2·10^{-5}$ bar O_2), 300mL_{STP}/min)

From the CFD model it was also possible to determine the contribution of the different resistances in dependence of thickness and temperature. Figure 7 shows the relative distribution of the different resistances in a thickness range from 10 to 10000 μm at 1000, 850 and 700 °C. As it can be seen and as it was previously mentioned, for thicknesses below 100 μm the bulk resistance effect is not significant in comparison with the gas-exchange surface resistances in both feed and sweep sides for all the considered temperatures. Concerning the contribution of the surface resistances, there is a stronger limiting effect of sweep side surface exchange reactions at higher temperatures and low thicknesses, whereas at lower temperatures the surface reactions at feed side become more dominant. The latter is due to oxygen reduction reactions occurring at feed side are more dependent on temperature, being then slower at low temperatures with respect to oxygen oxidation reactions [71–75]. The state-of-the-art BSCF asymmetric membranes considered for practical applications present thicknesses in the range from 10 to 70 μm, therefore it is necessary the conduction of surface activation strategies for optimizing the O_2 permeation performance [7,76]. For the highest thickness values studied, the bulk resistance becomes comparable to the surface resistances. At 700 °C (Figure 7a) and 850 °C (Figure 7b), the resistances of the three contributions are similar, while at 1000 °C (Figure 7c), the surface resistance on sweep side represents almost half of the total resistance. Other authors have reported similar resistance distribution [13,62].

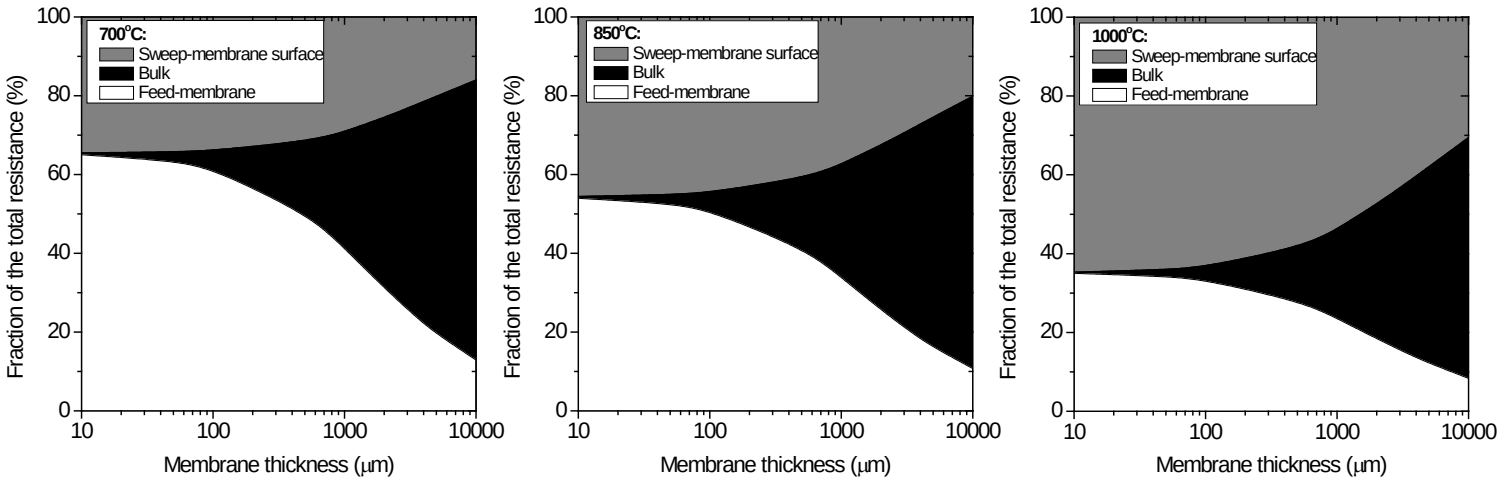

Figure 7. Contribution of the different resistances to the total resistance to oxygen permeation (a) 700 °C, (b) 850 °C, (c) 1000 °C. Feed inlet flow 300mL$_{STP}$/min, feed inlet: air, sweep inlet flow 300mL$_{STP}$/min, sweep inlet: Ar ($2 \cdot 10^{-5}$ bar O_2)

4.2 Effect of feed flow

Figure 8 shows the effect of feed flow rate in J_{O2} for a 0.8 mm-thick BSCF membrane at different temperatures. For the considered membrane thickness, as it was observed in the Figure 7, both the gas-exchange surface and the bulk resistances are in the same order of magnitude. As can be seen in Figure 8, the influence of feed flow rate is significant at low values, with a sharp J_{O2} decrease below 100 mL$_{STP}$/min for all the considered temperatures, whereas at flow rates above this value the O_2 fluxes are barely improved. This is due to concentration polarization phenomena occurring at feed side surface when the provided O_2 is insufficient for satisfying the high transport of O^{2-} through the bulk. Therefore, for high-permeating materials such as BSCF, if the amount of O^{2-} transported through the oxygen vacancies is higher than the supplied O_2 (this happening at low feed flows), then a significant decrease of the local pO_2 occurs at the membrane feed side surface due to an O_2 depletion in the gas phase. This produces a reduction in the driving force through the membrane and subsequently in the O_2 permeation. Instead, at higher feed flow rates, the O_2 supply is sufficiently high for ensuring the O^{2-} bulk diffusion and therefore no significant gain in J_{O2} is obtained by increasing the feed flow. This polarization concentration resistance takes place at all the temperatures, but it is more limiting at higher temperatures due to the higher O^{2-} bulk diffusion, as can be seen for the 1000 °C results. The same behavior was reported for Zhu et. al.[13] and Wang et al. [66].

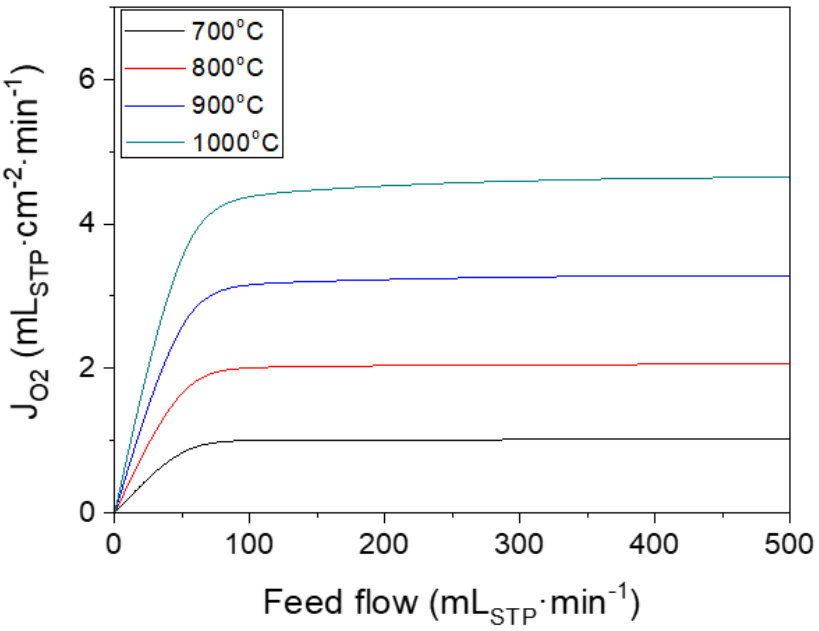

Figure 8: Effect of the feed inlet flow on the average oxygen flux for different temperatures. (Feed conditions: air , Sweep inlet conditions : Ar ($2 \cdot 10^{-5}$ bar O_2) 300 mL_{STP}/min, membrane thickness: 0.8mm)

4.3 Effect of the sweep inlet flow:

Similarly to the feed side, the permeate side is also affected by concentration polarization resistances in the way that an accumulation of O_2 on membrane surface generates an increase in the pO_2 thus lowering the pO_2 gradient across the membrane and, as previously explained, the J_{O2}. Such an accumulation arises from a poor O_2 desorption from the membrane surface due to an inefficient sweeping. The sweep inlet flow causes velocity gradients –on the membrane surface– that depend on the module geometry. The gas velocity gradients determine the O_2 concentration profile in the sweep gas compartment that, at the same time, influence the oxygen transport. Therefore, it is of great importance to study the effect of the sweep flow rates on the pO_2 profiles for understanding its influence on the maximization of J_{O2}. Figure 9 shows the effect of the sweep inlet flow on the average O_2 flux, the average pO_2 and the average shear rate on the membrane surface. The pO_2 is calculated as the average values at 2 mm from the membrane surface. From the obtained results it is confirmed that, as the sweep inlet flow rate increases, the O_2 in the sweep compartment is more diluted, and therefore, the J_{O2} increases as a consequence of the increased driving force. For sweep gas flow rates greater than 300 mL_{STP}/min (approximately 10^4 s^{-1} of average shear rate), the sweep inlet flow does not significantly influence the oxygen flux, thus setting the optimal value for 0.8 mm-thick BSCF membranes.

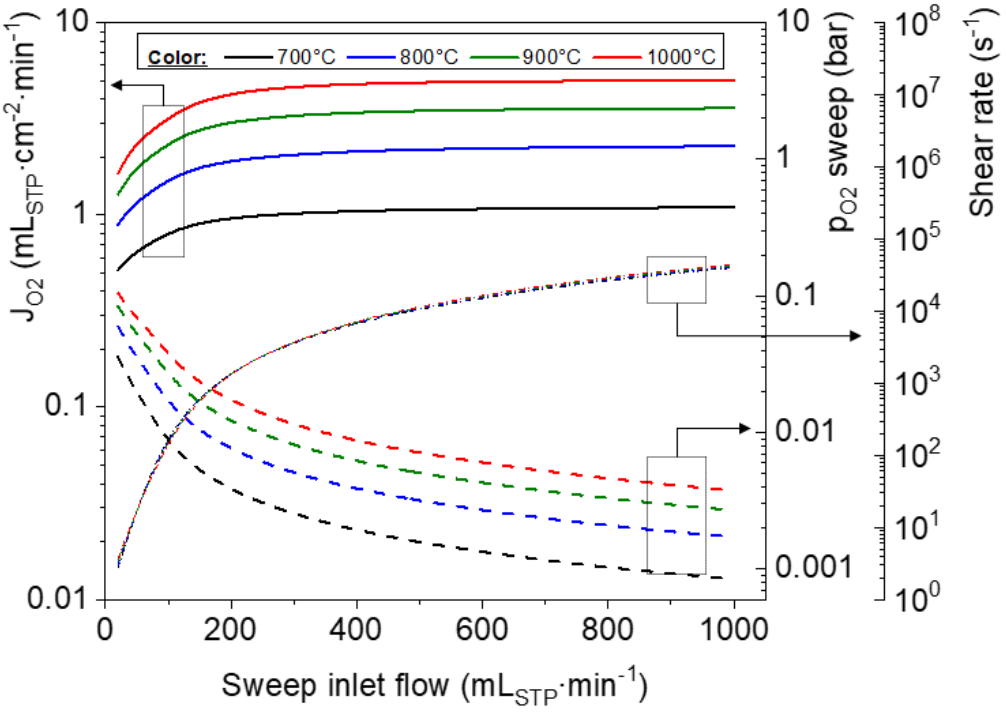

Figure 9: Effect of the sweep flow on the average oxygen flux, oxygen partial pressure over the membrane surface and shear rate at the reference conditions (Q_{feed} = 300 mL$_{STP}$·min^{-1}).

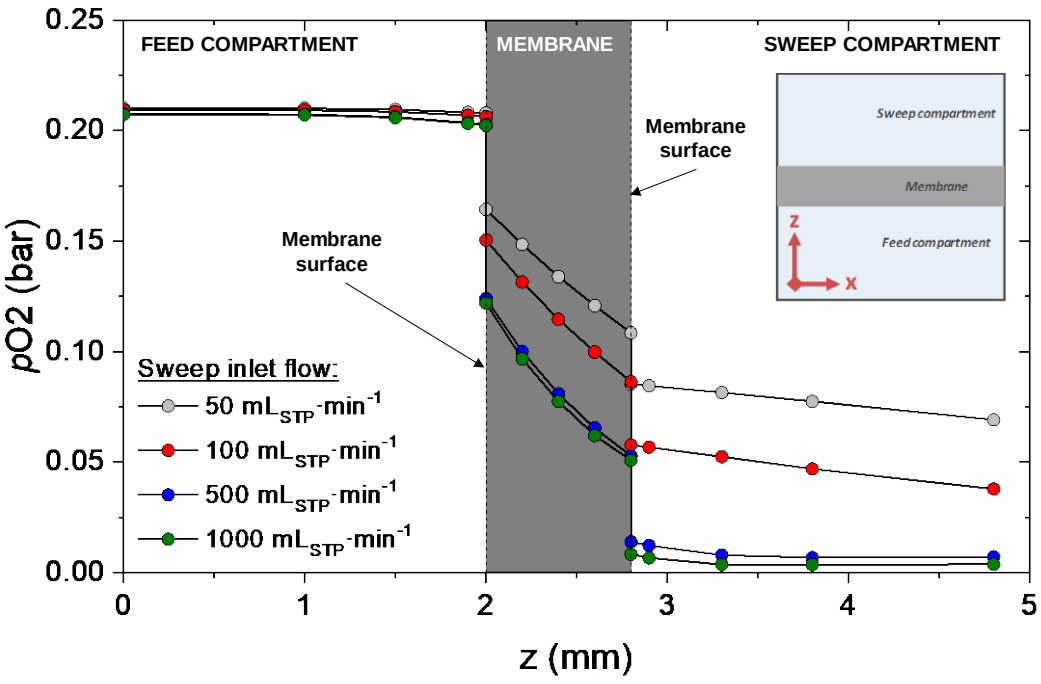

Figure 10: Oxygen partial pressure profile as a function of z coordinate at different sweep inlet flows and 1000 °C at reference conditions (Q_{feed} = 300 mL$_{STP}$·min^{-1}).

Figure 10 shows the pO_2 profile for different sweep inlet flows at 1000 °C. Regarding the pO_2 in the feed compartment, the polarization effects were not significant, even for the highest sweep inlet flows studied. However, in the sweep compartment, the polarization effect is important at low sweep inlet flows, since (i) the sweep stream does not dilute sufficiently the permeated O_2 and (ii) the velocity close to the membrane is not high enough to sweep the O_2 and to properly mix it with the main gas stream.

4.4 Analysis of the apparent activation energy

Taking into account the previous results, the effect of the thickness in the apparent activation energies related to the O_2 flux was studied for three cases according to the fluid dynamic regime: (i) the reference case; (ii) a case with low concentration polarization; and (iii) a case with high concentration polarization. The conditions of each case are described in Table 5.

Table 5: Conditions for the activation energies study

Case	**Feed inlet flow**	**Feed inlet**	**Sweep inlet flow**	**Sweep inlet O_2**
Units	mL_{STP}/min	-	mL_{STP}/min	*Bar*
Reference	300	Air	300	$2 \cdot 10^{-5}$
Low polarization	300	Air	500	$2 \cdot 10^{-5}$
High polarization	50	Air	50	$2 \cdot 10^{-5}$

Figure 11 shows the O_2 flux for three different membrane thicknesses (10, 100 and 1000 microns) in dependence of temperature. It is commonly found that the apparent activation energies (E_A) for oxygen permeation change their values above a certain temperature [19,77,78]. In our case, the results showed a change in E_A at a temperature near 800 °C.

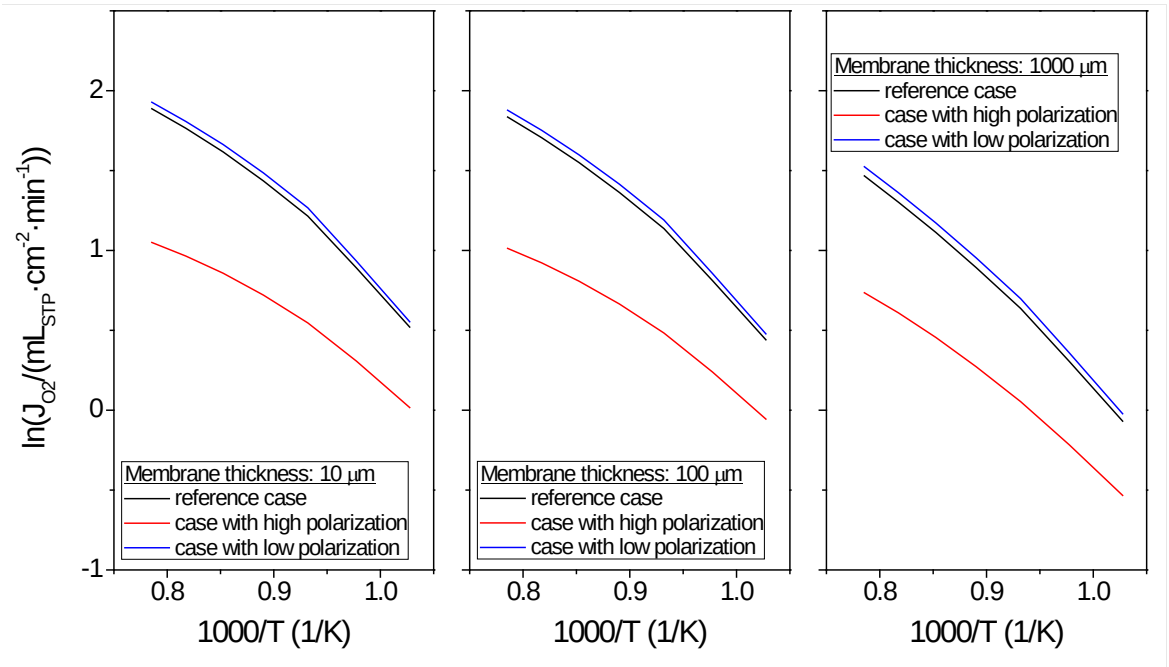

Figure 11: Oxygen flux. Feed inlet: air, sweep inlet: Ar ($2 \cdot 10^{-5}$ bar O_2). R = Reference case, LP = case with low gas-concentration polarization, HP = case with high gas-concentration polarization

Figure 12 shows the results of the E_A for the considered cases. The case with high polarization has the lowest E_A values, while the reference case and the case with low polarization present similar results. For all cases, E_A is lower at high temperatures (HT) than at lower temperatures (LT). At LT, the E_A for the reference and low polarization cases do not significantly vary with the membrane thickness, while for the high polarization case, it increases with the membrane thickness (specially above of 100 µm). At HT, there is a notable raise in the E_A with the thickness. These results are in line with previous experimental works [13,62] and enables to quickly interpret typical experimental results in O_2 permeation.

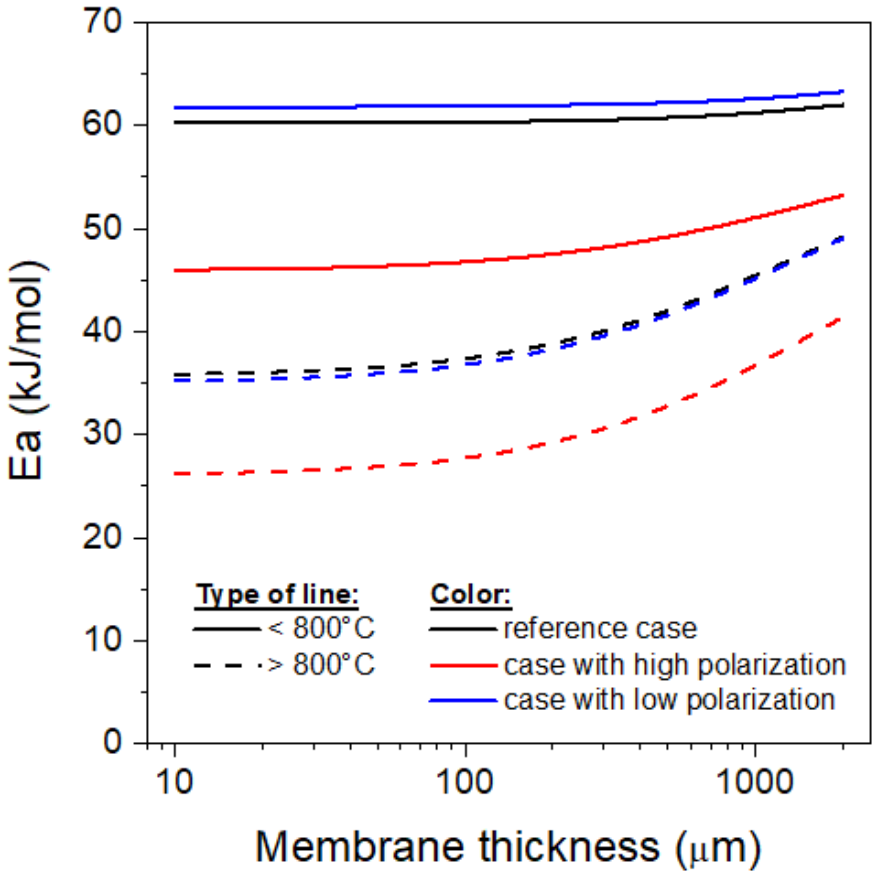

Figure 12: Apparent activation energies at LT (low temperature, <800 °C) and at HT (high temperature, >800 °C) for different cases, including the effect of gas-concentration polarization. Feed inlet: air, sweep inlet: Ar ($2 \cdot 10^{-5}$ bar O_2).

Figure 13 compares the pO_2 profiles for the high and low polarization cases. In Figure 13.a (high polarization case) a large pO_2 gradient can be observed in the sweep compartment near the membrane surface. Furthermore, the O_2 profile in the feed compartment shows that the permeated O_2 causes the pO_2 in contact with the membrane to be 12% lower than the pO_2 in the inlet feed. Otherwise, Figure 13.b (low polarization case) shows that the pO_2 on the membrane surface has practically the same value than in the feed. In this case, the streamlines indicate the formation a swirl close to the membrane.

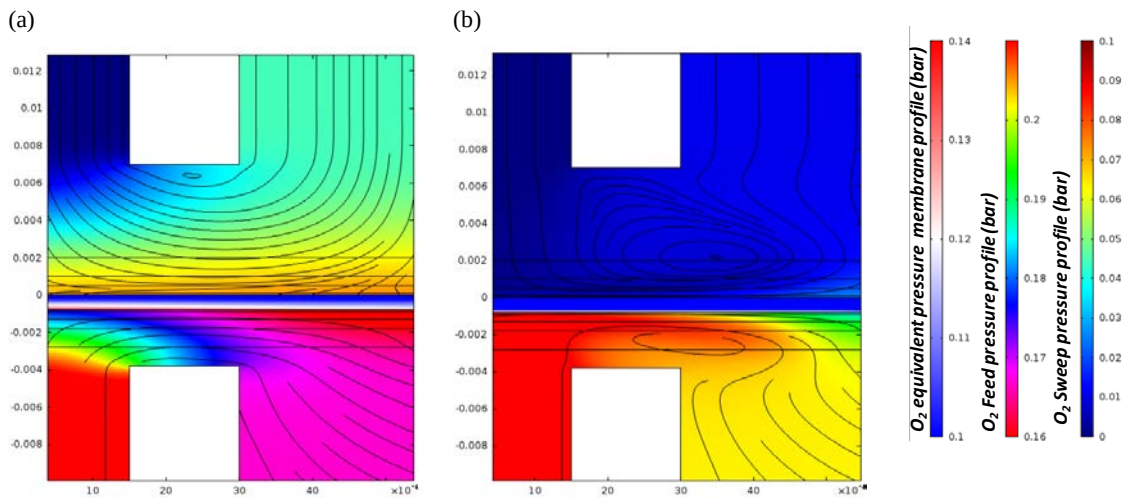

Figure 13: Oxygen pressure profile for the high polarization case (a) and the low polarization case (b) at 1000 °C. Streamlines: speed pathways.

4.5 Effect of the sweep gas composition on the oxygen transport in the gas phase

Considering the model established from the experimental data (obtained by using Ar as sweep), the effect of varying the type of sweep gas on the O_2 transport in the gas phase was studied. For conducting this study, the sweeping of a BSCF membrane with Ar, CO_2, H_2O and He was considered. Note that the possible effects on the surface resistance due to gas composition are not considered in the study (e.g., CO_2 and H_2O competitive adsorption on the surface of ionic membrane), i.e., only the fluid dynamic and diffusional characteristics are considered. Figure 14a shows the results of O_2 flux at different temperatures and sweep inlet flow for the four gases studied. The O_2 flux obtained using He as sweep is lower than that obtained with the other gases for values of sweep inlet flow higher than 100 mL_{STP}/min, whilst the J_{O2} tends to the same value for all gases at very high values of sweep gas flow. As the molecular mass of He is notably smaller than the other considered gases, therefore its 'sweeping capacity' is also smaller. This is because the sweeping of the O_2 molecules adsorbed on membrane surface not only depends on the diffusive effects generated by the low pO_2 induced by the sweep gas, but also on the fluid dynamic effect consisting of molecular collisions between sweep gas molecules and the adsorbed O_2 molecules. Therefore, the larger the molecules colliding with the adsorbed O_2 the better the sweeping will be. The viscosity of the sweep gas also influences this mechanism, i.e., the more viscous the fluid is the more the friction against the surface will produce. Therefore, sweep gases inducing a higher friction on membrane surface will release of adsorbed O_2 molecules more effectively and, subsequently, a better sweeping is reached. This is described by the shear rate, which quantifies the rate at which a fluid is sheared during flow. Figure 14b shows the shear rate on the membrane surface from the same simulations as an indicator of the 'sweeping capacity' in the way that the higher the shear rate the more effective the sweeping. At low sweep gas flows (high concentration polarization), all gases lead to similar shear rate values, but at high sweep

flow values (low gas-concentration polarization), the use of Ar, CO_2 or steam leads to shear rates two orders of magnitude higher than those of He, thus explaining the J_{O2} results observed in Figure 14a.

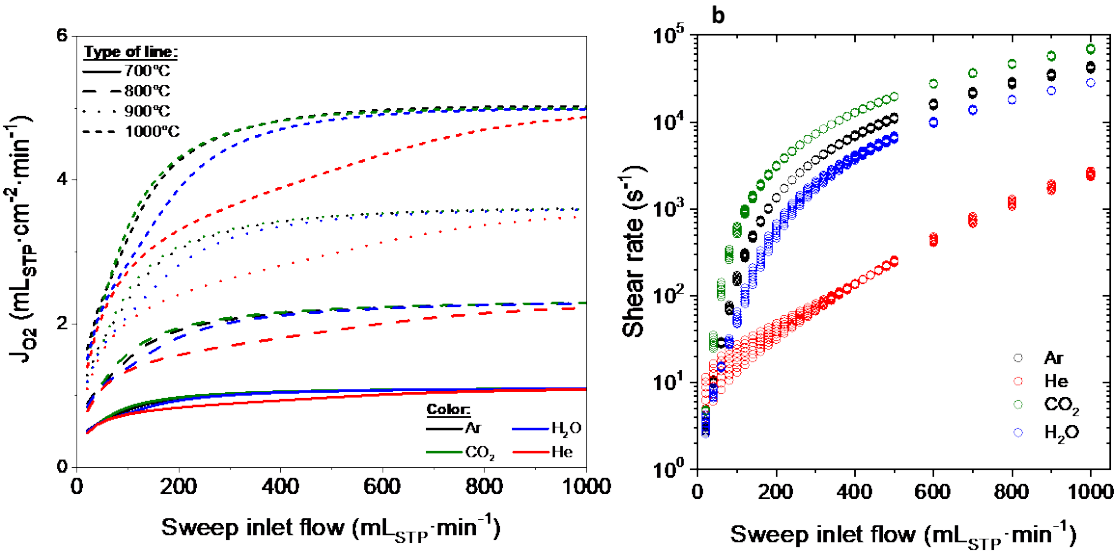

Figure 14. (a) Oxygen flux for different sweep gases (reference case) (b) shear rate in the sweep – membrane surface using different sweep gases (different sweep gas flow at reference conditions)

Finally, Figure 15 shows results of fitting the correlation between Sherwood (*Sh*), Reynolds (*Re*) and Schmidt (*Sc*) numbers (Eq 23). This plot shows the relation Sh/Sc^c, with c = 1/3 depending on Reynolds number, as expected for a gas separation process [52–57]. This plot provides an idea about the effect of the inertial forces effect on the permeation. At Reynolds lower than around 8 – 10, the inertial forces do not present any effect in the oxygen transport, thus for these lower values, the oxygen transport is due only for the difference of partial pressures and it is expected polarization close of the membrane appear due to that low inertial strength of the gas. At Reynolds higher than 8 – 10, the increase of the inertial forces in the gas improves the oxygen transference and, as consequence, the inertial forces enable to improve the sweeping of the oxygen permeated.

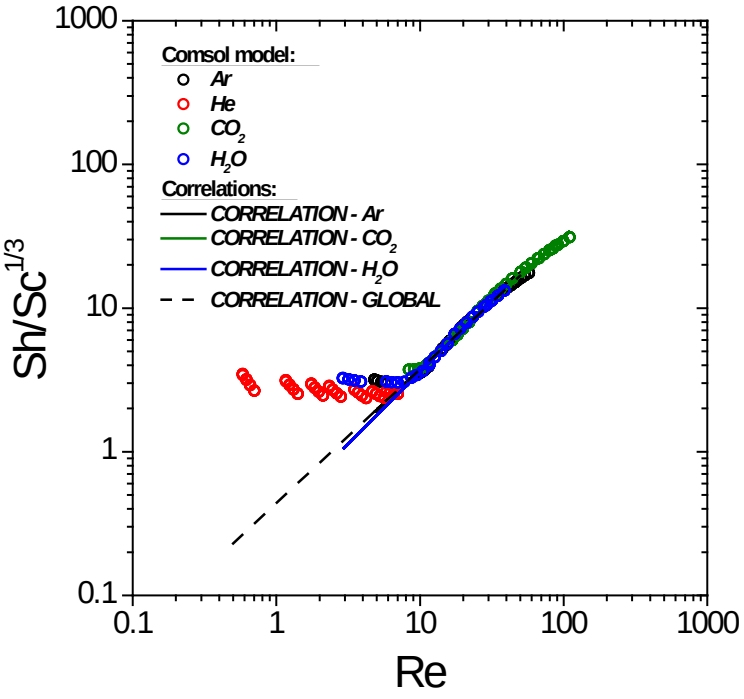

Figure 15. Evaluation of the fluid dynamic effect in the oxygen permeation using correlations of Sherwood, Reynolds and Schmidt dimensionless numbers.

Table 6 shows the comparison of the values for the fluid dynamic correlation for this study (before the fitting and after the fitting). The correlation values are in line with those reported elsewhere while the fitted constants are similar to the reported in the bibliography [52,53,55,56] using this correlation (Eq (23)).

Table 6. Comparison of the values for the fluid dynamic correlation (Eq. (23)).

Composition	**a**	**b**	**c**
O_2 - Ar	0.4361	0.9318	1/3
O_2 - steam	0.3577	1.0026	1/3
O_2 - CO_2	0.5121	0.8936	1/3
O_2 – Global (sweep)	0.4394	0.9323	1/3
O_2 – Air (feed)	0.5309	0.697	1/3

However, and although it is expected that the dilution has a higher effect in the O_2 permeation than the inertial effect (or sweep effect), this analysis reveals the importance of the sweep gas in the oxygen transport process. Therefore, in order to avoid polarizations in this chamber, the suitable gas compositions and flow shall be chosen carefully. These considerations could be critical when upscaling the permeation system to minimize the required membrane surface area, and thus the related capital expenses.

4.6 Vacuum system

Finally, the performance of a vacuum system was compared with that of case using sweep gas at an inlet flow for which low concentration polarization is obtained (500 mL_{STP}/min). Figure 16a shows that similar O_2 flux values to those of the sweep gas case are obtained for a vacuum pressure of 10 mbar. For this vacuum pressure, the O_2 flux is higher than that of the sweep gas case at temperatures higher than 800 °C and smaller under this temperature. The reason of this behavior can be seen in Figure 16b. Under this temperature value, the average pO_2 on the membrane surface is higher using vacuum pressure and, consequently, the driving force is smaller. In addition, compared with the situations in which a sweep gas is used, there are no significant changes in the pO_2 (Figure 16b) if vacuum pressure is used. A previous work reported similar results for tubular devices [66].

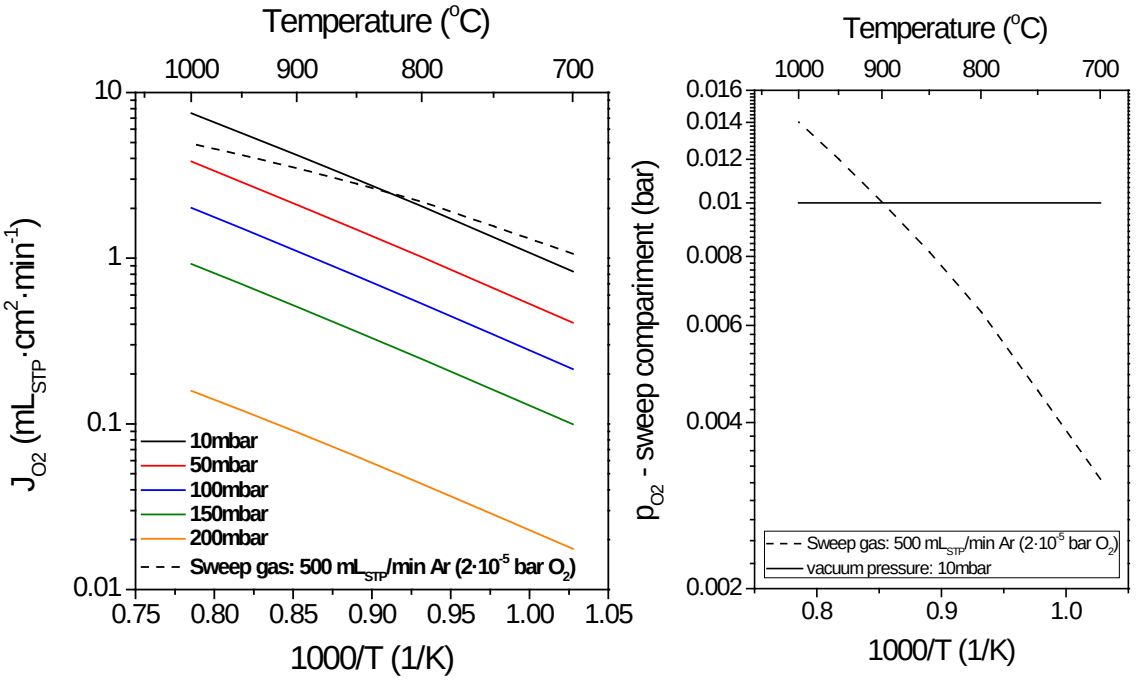

Figure 16: Vacuum results. (a) Oxygen flux results; (b) oxygen partial pressure in the sweep compartment. Feed inlet flow: 300mL_{STP}/min; feed inlet: air; thickness: 0.8mm

Figure 17 shows the pO_2, velocity profiles and streamlines for a vacuum pressure of 10 mbar at 1000 °C. Comparing the pO_2 profiles (Figure 17a) with one obtained using sweep gas, it can be observed that the vacuum systems achieve a more homogeneous O_2 profile in the sweep compartment. Therefore, by using vacuum pressure there is not stagnant flow near the corners and the entire membrane surface is active for transport.

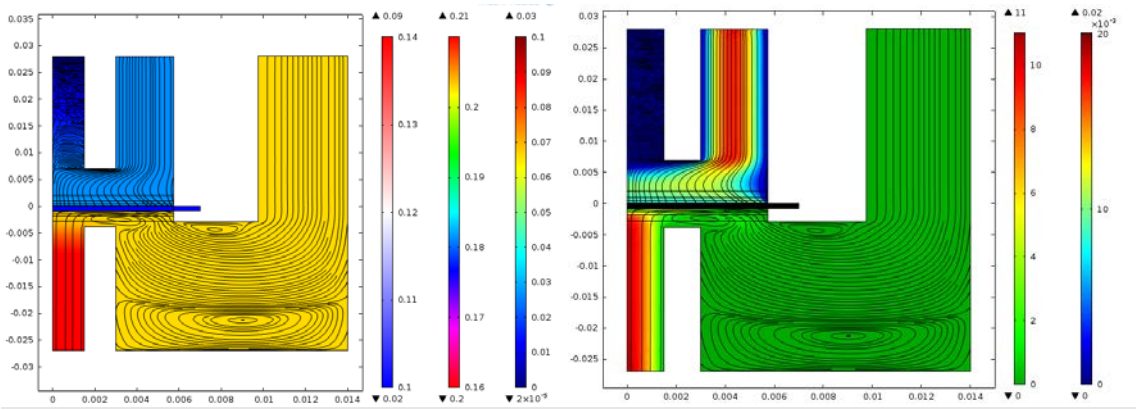

Figure 17: contour plots. (a) oxygen partial pressure profile (left bar: pressure profile in the vacuum compartment; middle bar: oxygen partial pressure in the feed compartment; right bar: oxygen equivalent pressure in the membrane; streamlines: speed pathways); (b) speed profile (left bar: oxygen flow profile in the membrane; middle bar: speed profile in the feed compartment; right bar: speed profile in the vacuum compartment; streamlines: speed pathways). Feed inlet flow: 500 mL_{STP}/min; feed inlet: air; vacuum pressure: 50 mbar; 1000 °C.

5 Conclusions

A finite element model was built to evaluate the oxygen transport across MIEC ceramics at high temperature. This methodology allows to perform a local evaluation of all the phenomena involved on the oxygen permeation process. A fitting of the model to experimental results was done to determine surface and bulk diffusion parameters. Whilst conventional 0D methodology can be influenced by polarization phenomena, the methodology considered in this study evaluates locally all the phenomena.

The results of the complete CFD model showed that the oxygen permeation of membrane with thicknesses >2mm are limited by bulk diffusion mechanism. Polarization effect causes strong limitations on the oxygen transport, especially at the sweep side. This polarization can occur at the sweep chamber when the permeated oxygen is not properly swept from the membrane surface. Furthermore, the inefficient sweeping is related to the nature of the gas used since it influences the diffusion of adsorbed oxygen species and desorption of molecular oxygen from the surface. This is related to two main factors that govern the inertial force of the sweep gas: (i) the speed of the gas close to the membrane; (ii) the molecular weight of the inert gas. The higher the both factors are (velocity and molecular weight), the better the oxygen is swept. The present study reveals that, although the diluting effect of the sweep gas strongly influences the oxygen transport, the sweeping effect is not negligible (mainly due to the appearance of polarization problems). Finally, a comparison with vacuum extraction of the oxygen permeated was performed. This last study allows evaluating how high vacuum pressures are needed to achieve similar oxygen results than when using a sweep gas.

6 Nomenclature

A_p	Pre-exponential factor of the permeate-membrane surface resistance
A_v	Pre-exponential factor of the diffusion coefficient of oxygen vacancies
A_{mod}	Membrane active area
$C_{Vö}$	Molar concentration of oxygen vacancies
C_i	Coefficients for equilibrium equation
$D_{Vö}$	Diffusion coefficient of oxygen vacancies
$E_{a,f}$	Activation energy factor of the feed-membrane surface resistance
$E_{a,p}$	Activation energy of the permeate-membrane surface resistance
$E_{a,v}$	Activation energy of the diffusion coefficient of oxygen vacancies
F	Faraday constant
j_{O2}	Molar flux of oxygen
$j_{Vö}$	Molar flux of oxygen vacancies
k	Mass-transfer coefficient
K	Temperature dependent coefficient of the oxygen non-stoichiometry
m	Temperature dependent exponent of the oxygen non-stoichiometry
n	Exponential coefficient for oxygen pressure dependence of surface resistance
N	Number of experiments
$\vec{p}$	Vector of parameters to be fitted
p_{O2}	Oxygen partial pressure
P_0	Reference pressure

Q_p	inlet flow of sweep gas
R	Universal gas constant
r_f	resistance parameter at the feed-membrane surface
r_p	resistance parameter at the permeate-membrane surface
$r_{f,0}$	Pre-exponential factor of surface resistance at the feed-membrane surface
$r_{p,0}$	Pre-exponential factor of surface resistance at the permeate-membrane surface
T	Absolute temperature
$\vec{y}$	Vector of experimental conditions
v_{BSCF}	Molar volume of BSCF membrane

Greek letters

Δ	Oxygen non-stoichiometry
Δz	Membrane thickness
μ_{O2}	Oxygen chemical potential

Subscripts

F	Feed side
P	Permeate side
Z	z-direction (perpendicular to the membrane plane)

Superscripts

*	Gas property calculated in equilibrium with the oxygen vacancies
S	Gas-membrane surface

7 Acknowledgments

This work was financially supported by Spanish Government (Grants SEV-2016-0683 and RTI2018-102161) and Generalitat Valenciana (PROMETEO/2018/006).

8 Bibliography

[1] M.A. Habib, H.M. Badr, et al., A review of recent developments in carbon capture utilizing oxy-fuel combustion in conventional and ion transport membrane systems, Int. J. Energy Res. 35 (2011) 741–764. doi:10.1002/er.1798.

[2] S.S. Hashim, A.R. Mohamed, et al., Oxygen separation from air using ceramic-based membrane technology for sustainable fuel production and power generation, Renew. Sustain. Energy Rev. 15 (2011) 1284–1293. doi:10.1016/J.RSER.2010.10.002.

[3] P. Markewitz, J. Marx, et al., Ecological Evaluation of Coal-fired Oxyfuel Power Plants - cryogenic Versus Membrane-based Air Separation-, Energy Procedia. 37 (2013) 2864–2876. doi:10.1016/J.EGYPRO.2013.06.172.

[4] M. Puig-Arnavat, S. Soprani, et al., Integration of mixed conducting membranes in an oxygen–steam biomass gasification process, RSC Adv. 3 (2013) 20843. doi:10.1039/c3ra44509g.

[5] S. Smart, C.X.C. Lin, et al., Ceramic membranes for gas processing in coal gasification, Energy Environ. Sci. 3 (2010) 268. doi:10.1039/b924327e.

[6] R. Castillo, Thermodynamic analysis of a hard coal oxyfuel power plant with high temperature three-end membrane for air separation, Appl. Energy. 88 (2011) 1480–1493. doi:10.1016/J.APENERGY.2010.10.044.

[7] S. Baumann, J.M. Serra, et al., Ultrahigh oxygen permeation flux through supported Ba0.5Sr0.5Co0.8Fe0.2O3−δ membranes, J. Memb. Sci. 377 (2011) 198–205. doi:10.1016/J.MEMSCI.2011.04.050.

[8] M.J. den Exter, W.G. Haije, et al., Viability of ITM Technology for Oxygen Production and Oxidation Processes: Material, System, and Process Aspects, in: Inorg. Membr. Energy Environ. Appl., Springer New York, New York, NY, 2009: pp. 27–51. doi:10.1007/978-0-387-34526-0_2.

[9] S. Engels, F. Beggel, et al., Simulation of a membrane unit for oxyfuel power plants under consideration of realistic BSCF membrane properties, J. Memb. Sci. 359 (2010) 93–101. doi:10.1016/J.MEMSCI.2010.01.048.

[10] Z. Shao, W. Yang, et al., Investigation of the permeation behavior and stability of a Ba0.5Sr0.5Co0.8Fe0.2O3−δ oxygen membrane, J. Memb. Sci. 172 (2000) 177–188.

doi:10.1016/S0376-7388(00)00337-9.

[11] M. Arnold, H. Wang, et al., Influence of CO2 on the oxygen permeation performance and the microstructure of perovskite-type (Ba0.5Sr0.5)(Co0.8Fe0.2)O3−δ membranes, J. Memb. Sci. 293 (2007) 44–52. doi:http://dx.doi.org/10.1016/j.memsci.2007.01.032.

[12] J. Yi, M. Schroeder, High temperature degradation of Ba0.5Sr0.5Co0.8Fe0.2O3−δ membranes in atmospheres containing concentrated carbon dioxide, J. Memb. Sci. 378 (2011) 163–170. doi:10.1016/j.memsci.2011.04.044.

[13] X. Zhu, H. Liu, et al., Permeation model and experimental investigation of mixed conducting membranes, AIChE J. 58 (2012) 1744–1754. doi:10.1002/aic.12710.

[14] K. Gerdes, D. Luss, Oxygen transport model for layered MIEC composite membranes, Solid State Ionics. 177 (2006) 2931–2938. doi:10.1016/J.SSI.2006.09.002.

[15] H. Xie, Y. Wei, et al., Modeling of U-shaped Ba0.5Sr0.5Co0.8Fe0.2O3−δ hollow-fiber membrane for oxygen permeation, Chinese J. Chem. Eng. 25 (2017) 892–897. doi:10.1016/J.CJCHE.2017.02.002.

[16] Y. Zhu, W. Li, et al., Selection of oxygen permeation models for different mixed ionic-electronic conducting membranes, AIChE J. 63 (2017) 4043–4053. doi:10.1002/aic.15718.

[17] C. Li, J.J. Chew, et al., Modelling of oxygen transport through mixed ionic-electronic conducting (MIEC) ceramic-based membranes: An overview, J. Memb. Sci. 567 (2018) 228–260. doi:10.1016/J.MEMSCI.2018.09.016.

[18] Y.-S. Lin, W. Wang, et al., Oxygen permeation through thin mixed-conducting solid oxide membranes, AIChE J. 40 (1994) 786–798. doi:10.1002/aic.690400506.

[19] S.J. Xu, W.J. Thomson, Oxygen permeation rates through ion-conducting perovskite membranes, Chem. Eng. Sci. 54 (1999) 3839–3850. doi:10.1016/S0009-2509(99)00015-9.

[20] B. Zydorczak, K. Li, et al., Mixed conducting membranes - Macrostructure related oxygen permeation flux, AIChE J. 56 (2010) 3084–3090. doi:10.1002/aic.12216.

[21] S. Li, W. Jin, et al., Synthesis and oxygen permeation properties of La0.2Sr0.8Co0.2Fe0.8O3−δ membranes, Solid State Ionics. 124 (1999) 161–170. doi:10.1016/S0167-2738(99)00136-8.

[22] Z. Wang, H. Liu, et al., Improvement of the oxygen permeation through perovskite hollow fibre membranes by surface acid-modification, J. Memb. Sci. 345 (2009) 65–73. doi:10.1016/J.MEMSCI.2009.08.024.

[23] H. Pan, L. Li, et al., Improvement of oxygen permeation in perovskite hollow fibre membranes by the enhanced surface exchange kinetics, J. Memb. Sci. 428 (2013) 198–204. doi:10.1016/J.MEMSCI.2012.10.020.

[24] A. Ghadimi, M.A. Alaee, et al., Oxygen permeation of BaxSr1 − xCo0.8Fe0.2O3 − δ perovskite-type membrane: Experimental and modeling, Desalination. 270 (2011) 64–75. doi:http://dx.doi.org/10.1016/j.desal.2010.11.022.

[25] S. Kim, Y.L. Yang, et al., Oxygen surface exchange in mixed ionic electronic conductor membranes, Solid State Ionics. 121 (1999) 31–36. doi:10.1016/S0167-2738(98)00389-0.

[26] B. Van Hassel, T. Kawada, et al., Oxygen permeation modelling of perovskites, Solid State Ionics. (1993). doi:10.1016/0167-2738(93)90419-4.

[27] Y. Jin, Z. Rui, et al., Sequential simulation of dense oxygen permeation membrane reactor for hydrogen production from oxidative steam reforming of ethanol with ASPEN PLUS, Int. J. Hydrogen Energy. 35 (2010) 6691–6698. doi:10.1016/J.IJHYDENE.2010.04.042.

[28] N.D. Mancini, S. Gunasekaran, et al., A Multiple-Compartment Ion-Transport-Membrane Reactive Oxygen Separator, Ind. Eng. Chem. Res. 51 (2012) 7988–7997. doi:10.1021/ie202433g.

[29] D.M. Turi, P. Chiesa, et al., High fidelity model of the oxygen flux across ion transport membrane reactor: Mechanism characterization using experimental data, Energy. 96 (2016) 127–141. doi:10.1016/J.ENERGY.2015.12.055.

[30] N.D. Mancini, A. Mitsos, Ion transport membrane reactors for oxy-combustion – Part I: intermediate-fidelity modeling, Energy. 36 (2011) 4701–4720. doi:10.1016/J.ENERGY.2011.05.023.

[31] V. Spallina, T. Melchiori, et al., Auto-Thermal Reforming Using Mixed Ion-Electronic Conducting Ceramic Membranes for a Small-Scale H2 Production Plant, Molecules. 20 (2015) 4998–5023. doi:10.3390/molecules20034998.

[32] C.D. Fischer, O.A. Iribarren, Oxygen integration between a gasification process and oxygen production using a mass exchange heuristic, Int. J. Hydrogen Energy. 41 (2016) 2399–2410. doi:10.1016/J.IJHYDENE.2015.12.124.

[33] A. Hunt, G. Dimitrakopoulos, et al., Measuring the oxygen profile and permeation flux across an ion transport (La0.9Ca0.1FeO3−δ) membrane and the development and validation of a multistep surface exchange model, J. Memb. Sci. 468 (2014) 62–72. doi:10.1016/J.MEMSCI.2014.05.043.

[34] J. Hong, P. Kirchen, et al., Numerical simulation of ion transport membrane reactors:

Oxygen permeation and transport and fuel conversion, J. Memb. Sci. 407–408 (2012) 71–85. doi:10.1016/J.MEMSCI.2012.03.018.

[35] M.A. Habib, R. Ben Mansour, et al., Modeling of oxygen permeation through a LSCF ion transport membrane, Comput. Fluids. 76 (2013) 1–10. doi:10.1016/J.COMPFLUID.2013.01.007.

[36] M.A. Nemitallah, A study of methane oxy-combustion characteristics inside a modified design button-cell membrane reactor utilizing a modified oxygen permeation model for reacting flows, J. Nat. Gas Sci. Eng. 28 (2016) 61–73. doi:10.1016/J.JNGSE.2015.11.041.

[37] M.A. Nemitallah, M.A. Habib, et al., Experimental and numerical study of oxygen separation and oxy-combustion characteristics inside a button-cell LNO-ITM reactor, Energy. 84 (2015) 600–611. doi:10.1016/J.ENERGY.2015.03.022.

[38] P. Ahmed, M.A. Habib, et al., Investigation of oxygen permeation through disc-shaped BSCF ion transport membrane under reactive conditions, Int. J. Energy Res. 41 (2017) 1049–1062. doi:10.1002/er.3696.

[39] N. Kawachale, A. Kumar, et al., A flow distribution study of laboratory scale membrane gas separation cells, J. Memb. Sci. 332 (2009) 81–88. doi:10.1016/J.MEMSCI.2009.01.042.

[40] M. Coroneo, G. Montante, et al., Modelling the effect of operating conditions on hydrodynamics and mass transfer in a Pd–Ag membrane module for H2 purification, J. Memb. Sci. 343 (2009) 34–41. doi:10.1016/J.MEMSCI.2009.07.008.

[41] M. Coroneo, G. Montante, et al., Numerical and Experimental Fluid-Dynamic Analysis To Improve the Mass Transfer Performances of Pd−Ag Membrane Modules for Hydrogen Purification, Ind. Eng. Chem. Res. 49 (2010) 9300–9309. doi:10.1021/ie100840z.

[42] G. Ji, G. Wang, et al., Computational fluid dynamics applied to high temperature hydrogen separation membranes, Front. Chem. Sci. Eng. 6 (2012) 3–12. doi:10.1007/s11705-011-1161-5.

[43] G. Ji, J.G. Yao, et al., Enhanced hydrogen production from thermochemical processes, Energy Environ. Sci. 11 (2018) 2647–2672. doi:10.1039/C8EE01393D.

[44] G. Ji, M. Zhao, et al., Computational fluid dynamic simulation of a sorption-enhanced palladium membrane reactor for enhancing hydrogen production from methane steam reforming, Energy. 147 (2018) 884–895. doi:10.1016/J.ENERGY.2018.01.092.

[45] J. Wang, X. Gao, et al., CFD simulation of hollow fiber supported NaA zeolite membrane modules, Sep. Purif. Technol. 213 (2019) 1–10. doi:10.1016/J.SEPPUR.2018.12.017.

[46] G. Ji, G. Wang, et al., The fluid dynamic effect on the driving force for a cobalt oxide silica membrane module at high temperatures, Chem. Eng. Sci. 111 (2014) 142–152. doi:10.1016/J.CES.2014.02.006.

[47] J.M. Gozálvez-Zafrilla, A. Santafé-Moros, et al., Fluid dynamic modeling of oxygen permeation through mixed ionic-electronic conducting membranes, J. Memb. Sci. 378 (2011) 290–300. doi:10.1016/j.memsci.2011.05.016.

[48] R. Kriegel, R. Kircheisen, et al., Oxygen stoichiometry and expansion behavior of Ba0.5Sr0.5Co0.8Fe0.2O3 - δ, Solid State Ionics. (2010). doi:10.1016/j.ssi.2009.11.012.

[49] R.L. Haupt, S.E. Haupt, Practical genetic algorithms, John Wiley & Sons, Hoboken, New Jersey, 2004.

[50] J. Yi, M. Schroeder, et al., Behavior of Ba(Co, Fe, Nb)$O_{3-\delta}$ Perovskite in CO_2 -Containing Atmospheres: Degradation Mechanism and Materials Design, Chem. Mater. 22 (2010) 6246–6253. doi:10.1021/cm101665r.

[51] A. Leo, S. Liu, et al., Production of pure oxygen from BSCF hollow fiber membranes using steam sweep, Sep. Purif. Technol. 78 (2011) 220–227. doi:10.1016/J.SEPPUR.2011.02.006.

[52] S. LEE, Applicability of Sherwood correlations for natural organic matter (NOM) transport in nanofiltration (NF) membranes, J. Memb. Sci. 240 (2004) 49–65. doi:10.1016/j.memsci.2004.04.011.

[53] Makaka S., Aziz M., et al., Copper recovery in a bench-scale carrier facilitated tubular supported liquid membrane system, J. Min. Metall. Sect. B Metall. 46 (2010) 67–73. doi:10.2298/JMMB1001067M.

[54] J. Catalano, M. Giacinti Baschetti, et al., Influence of the gas phase resistance on hydrogen flux through thin palladium–silver membranes, J. Memb. Sci. 339 (2009) 57–67. doi:10.1016/j.memsci.2009.04.032.

[55] L. Giani, G. Groppi, et al., Mass-Transfer Characterization of Metallic Foams as Supports for Structured Catalysts, Ind. Eng. Chem. Res. 44 (2005) 4993–5002. doi:10.1021/ie0490886.

[56] G. Groppi, L. Giani, et al., Generalized Correlation for Gas/Solid Mass-Transfer Coefficients in Metallic and Ceramic Foams, Ind. Eng. Chem. Res. 46 (2007) 3955–3958. doi:10.1021/ie061330g.

[57] R. Bird, W. Stewart, et al., Transport phenomena, (2007). https://books.google.com/books?hl=es&lr=&id=L5FnNlIaGfcC&oi=fnd&pg=PR13&ots

=LJg9g0mRsF&sig=IPC3N31e4f7wn05KrUVV9tCZWQE (accessed July 26, 2019).

[58] L. Wang, R. Merkle, et al., Oxygen tracer diffusion in dense Ba0.5Sr0.5Co0.8Fe0.2O3−δ films, Appl. Phys. Lett. 94 (2009). doi:http://dx.doi.org/10.1063/1.3085969.

[59] A. Berenov, A. Atkinson, et al., Oxygen tracer diffusion and surface exchange kinetics in Ba0.5Sr0.5Co0.8Fe0.2O3 − δ, Solid State Ionics. 268, Part (2014) 102–109. doi:http://dx.doi.org/10.1016/j.ssi.2014.09.031.

[60] M. Kessel, R.A. De Souza, et al., Oxygen diffusion in single crystal barium titanate, Phys. Chem. Chem. Phys. 17 (2015) 12587–12597. doi:10.1039/C5CP01187F.

[61] T. Antonini, K. Gallucci, et al., Oxygen transport by ionic membranes: Correlation of permeation data and prediction of char burning in a membrane-assisted biomass gasification process, Chem. Eng. Process. Process Intensif. 94 (2015) 39–52. doi:10.1016/j.cep.2014.11.009.

[62] A. Behrouzifar, A.A. Asadi, et al., Experimental investigation and mathematical modeling of oxygen permeation through dense Ba0.5Sr0.5Co0.8Fe0.2O3−δ (BSCF) perovskite-type ceramic membranes, Ceram. Int. (2012). doi:10.1016/j.ceramint.2012.02.068.

[63] D. Chen, Z. Shao, Surface exchange and bulk diffusion properties of Ba0.5Sr0.5Co0.8Fe0.2O3−δ mixed conductor, Int. J. Hydrogen Energy. 36 (2011) 6948–6956. doi:10.1016/j.ijhydene.2011.02.087.

[64] H. Wang, W. Yang, et al., Diffusion Fundamentals, Diffus. Fundam. (Online Journal). 1 (2005) 1–17. http://www.uni-leipzig.de/diffusion/contents_vol1.html.

[65] D. Gao, J. Zhao, et al., Influence of high-energy ball milling of the starting powder on the sintering; microstructure and oxygen permeability of Ba0.5Sr0.5Co0.5Fe0.5O3−δ membranes, J. Memb. Sci. (2011). doi:10.1016/j.memsci.2010.10.001.

[66] H. Wang, R. Wang, et al., Experimental and modeling studies on Ba0.5Sr 0.5Co0.8Fe0.2O3-δ (BSCF) tubular membranes for air separation, J. Memb. Sci. 243 (2004) 405–415. doi:10.1016/j.memsci.2004.07.003.

[67] S. Baumann, F. Schulze-Küppers, et al., Influence of sintering conditions on microstructure and oxygen permeation of Ba0.5Sr0.5Co0.8Fe0.2O3−δ (BSCF) oxygen transport membranes, J. Memb. Sci. (2010). doi:10.1016/j.memsci.2010.02.002.

[68] L. Tan, X. Gu, et al., Influence of powder synthesis methods on microstructure and oxygen permeation performance of Ba0.5Sr0.5Co0.8Fe0.2O3−δ perovskite-type membranes, J. Memb. Sci. (2003). doi:10.1016/S0376-7388(02)00494-5.

[69] J. Vente, S. McIntosh, et al., Properties and performance of BaxSr1−xCo0.8Fe0.2O3−δ

materials for oxygen transport membranes, J. Solid State Electrochem. (2006). doi:10.1007/s10008-006-0130-2.

[70] M.P. Popov, I.A. Starkov, et al., Improvement of Ba0.5Sr0.5Co0.8Fe0.2O3−δ functional properties by partial substitution of cobalt with tungsten, J. Memb. Sci. 469 (2014) 88–94. doi:10.1016/J.MEMSCI.2014.06.022.

[71] N. Mahato, A. Banerjee, et al., Progress in material selection for solid oxide fuel cell technology: A review, Prog. Mater. Sci. 72 (2015) 141–337. doi:10.1016/J.PMATSCI.2015.01.001.

[72] Z. Gao, L. V. Mogni, et al., A perspective on low-temperature solid oxide fuel cells, Energy Environ. Sci. 9 (2016) 1602–1644. doi:10.1039/C5EE03858H.

[73] S.B. Adler, Factors Governing Oxygen Reduction in Solid Oxide Fuel Cell Cathodes†, (2004). doi:10.1021/CR020724O.

[74] X. Zhang, L. Liu, et al., Enhanced Oxygen Reduction Activity and Solid Oxide Fuel Cell Performance with a Nanoparticles-Loaded Cathode, Nano Lett. 15 (2015) 1703–1709. doi:10.1021/nl5043566.

[75] C. Sun, R. Hui, et al., Cathode materials for solid oxide fuel cells: a review, J. Solid State Electrochem. 14 (2010) 1125–1144. doi:10.1007/s10008-009-0932-0.

[76] R. Hoffmann, U. Pippardt, et al., Impact of sintering temperature on permeation and long-term development of support structure and stability for asymmetric oxygen transporting BSCF membranes, J. Memb. Sci. 581 (2019) 270–282. doi:10.1016/J.MEMSCI.2019.03.066.

[77] M.P. Lobera, M. Balaguer, et al., Catalytic Oxide-Ion Conducting Materials for Surface Activation of $Ba_{0.5}Sr_{0.5}Co_{0.8}Fe_{0.2}O_{3-\delta}$ Membranes, ChemistrySelect. 2 (2017) 2949–2955. doi:10.1002/slct.201700530.

[78] J.M. Serra, J. Garcia-Fayos, et al., Oxygen permeation through tape-cast asymmetric all-La0.6Sr0.4Co0.2Fe0.8O3−δ membranes, J. Memb. Sci. 447 (2013) 297–305. doi:10.1016/J.MEMSCI.2013.07.030.